Uncooled CMOS terahertz imager using a metamaterial absorber and pn diode

IVONNE ESCORCIA,[1] JAMES GRANT,[1] JOHN GOUGH,[2] DAVID R. S. CUMMING[1,*]

[1]*Microsystem Technology Group, School of Engineering, University of Glasgow, G12 8LT, UK*
[2]*Texas Instruments, Greenock, PA16 0EQ, UK*
**Corresponding author: David.Cumming.2@glasgow.ac.uk*

Received XX Month XXXX; revised XX Month, XXXX; accepted XX Month XXXX; posted XX Month XXXX (Doc. ID XXXXX); published XX Month XXXX

We demonstrate a low-cost uncooled terahertz (THz) imager fabricated in a standard 180 nm CMOS process. The imager is composed of a broadband THz metamaterial absorber coupled with a diode microbolometer sensor where the pn junction is used as a temperature sensitive device. The metamaterial absorber array is integrated in the top metallic layers of a six metal layer process allowing for complete monolithic integration of the metamaterial absorber and sensor. We demonstrate the capability of the detector for stand-off imaging applications by using it to form transmission and reflection images of a metallic object hidden in a manila envelope.

OCIS codes: *(110.0110) Imaging systems; (040.2235) Far infrared or terahertz; (110.6795) Terahertz imaging; (160.3918) Metamaterials.*

http://dx.doi.org/10.1364/OL.41.003261

The unique characteristics of Terahertz (THz) waves have placed an important focus on the development of low-cost, portable and real-time THz imaging devices. THz waves are transparent to many non-conductive materials that are opaque in the visible and infrared (IR) regions making it an attractive modality for detecting hidden objects in stand-off imaging applications such as security portals [1]. Moreover, THz has the potential to detect illicit substances such as drugs because of their unique THz spectral signatures [2]. Medical imaging is also a potential application field due to the non-ionizing attributes of THz waves and ability to detect surface cancer in tissue without being harmful to skin [3,4].
The major limitations hampering the proliferation of these THz applications into everyday life are the lack of appropriate inexpensive, compact THz sources and detectors that can operate at room temperature. Over the last decade many THz sources and detectors have been studied [5-10]. Typical THz detectors include pyroelectric sensors, Schottky barrier diodes (SBDs), field effect transistors (FETs) and resistive microbolometers. Of these, only the FET and resistive microbolometer are suitable for scaling to large focal plane array sizes (e.g. 64 x 64 pixels) since they can be easily integrated with Complementary Metal Oxide Semiconductor (CMOS) technology where the addressing and signal amplification circuitry is readily available. Arrays of FETs are extremely attractive since the detector and antenna structure can be implemented entirely in the CMOS process presenting a very low-cost effective option [11,12]. However, to date, the sensitivities of FETs are not comparable to surface micro-machined microbolometers and moreover, the pixel sizes are relatively large. Micro-machined microbolometer technology has been successfully extrapolated from the IR region to the THz band by simply scaling the appropriate features [13,15]. A micro-bridge, consisting of the resistive microbolometer and a suitable absorber material or structure is formed on top of the CMOS integrated circuit (IC). The microbolometer detects the temperature change caused by the incident power on the pixel. This change produces an electrical signal where the voltage or current is measured by data acquisition systems. The most common method to absorb the THz radiation is to employ a quarter wavelength cavity however at THz frequencies the cavity size is greater than 10 μm, dramatically increasing the fabrication complexity and cost [13-15].
In this paper we present a CMOS compatible fully integrated THz detector. We use a THz metamaterial (MM) absorber to selectively absorb the THz radiation coupled with a silicon pn diode to detect the temperature change. The MM structure absorbs the radiation in a thickness of $\lambda/30$ overcoming the thickness limitation of the traditional quarter wavelength approach. Instead of costly and laborious surface micro-machining techniques to realize the micro-bridge above the IC the MM absorber is formed in the metal and dielectric layers of the CMOS process. Furthermore, instead of employing a resistive microbolometer that must be added in an additional processing step we use a silicon pn diode that is formed in the front end of the CMOS process. Such an approach, where the absorber structure and sensor are implemented directly in the CMOS process, dramatically reduces the fabrication complexity and cost compared to competing THz microbolometer imagers. Previous work has described a MM based CMOS THz imager where the MM absorber was embedded in the metal and dielectric layers and a vanadium oxide (VO_x) microbolometer was fabricated on top [16]. Subsequent work successfully scaled this single pixel approach to form pixel arrays [17]. In this paper we investigate the

use of a Si pn junction as an alternative thermal sensor to using a VO_x microbolometer.

The THz detector was fabricated in a 180 nm six metal layer CMOS process from Texas Instruments. The sensor array area was 1.5 mm x 1.5 mm with a pixel pitch of 30 µm. Each pixel contained a broadband MM absorber, comprised of three cross-shaped electric ring resonators (ERRs), and a microbolometer, composed of three diodes connected in series. The broadband MM absorber structure was based on that reported in [18,19]. Figure 1a shows a layout section of the fabricated THz imager (top array) and the layout of the diodes connected in series of a single pixel. The perspective view of the broadband MM absorber and diode microbolometer integrated in a standard n-well CMOS process is shown in Figure 1b with its respective color-coded legend corresponding to each CMOS layer. The diodes were located in the lower layers of the CMOS process (p+ and n-well), metal 1 (M1) and 2 (M2) layers were used to connect the pixels to output pads, metal 3 (M3) was the MM absorber ground plane and metals 4 to 6 (M4 - M6) were ERRs of differing sizes. All the metal layers were separated by intermetal dielectric.

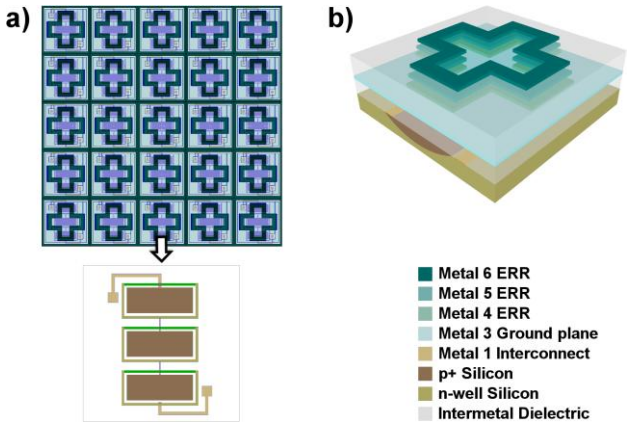

Fig. 1. a) Layout section of the fabricated THz detector (top array) and layout of the diodes connected in series of a single pixel. b) Perspective view of the diode pixel.

To minimize the membrane thickness and improve detector responsivity, by reducing both the thermal conductance and thermal capacitance, the passivation layer above M6 was removed by the foundry, and the silicon substrate was back-etched by post-processing steps. A standard SF_6/C_4F_8 plasma etch process was used to remove the majority of the silicon substrate. Two samples were etched: one where 50 µm of silicon remained (device A) and a second where only 1 µm remained (device B). Since there was ~ 8 µm of dielectric above the silicon this resulted in membrane thicknesses of 58 µm and 9 µm respectively. The unetched chip membrane thickness was 388 µm (device C). After etching, the CMOS chips were glued to ceramic carriers and wire bonded for characterization.

The refractive index of the materials that compose the broadband MM absorber and microbolometer sensor are shown in Figure 2a. The metallic layers with ERRs are shown in red, the dielectric insulating layers in light blue and the silicon substrate in yellow. 3D Finite Difference Time Domain (FDTD) simulations (Lumerical Inc.) were used to determine the spectral response and spatial absorption characteristics of the MM absorber. Fourier Transform Infrared (FTIR) Spectroscopy was used to experimentally determine the spectral response. Full details of the simulation and experimental strategy can be found in [18]. It was necessary that appreciable absorption, greater than 50%, was obtained at 2.52 THz, the operating frequency of the CO_2 pumped CH_3OH gas laser used in the detector characterization and imaging experiments. The simulation and experimental absorption results for the broadband MM absorber are shown in Figure 2b. The experimental data shows two absorption peaks at 2.78 THz and 2.52 THz with an absorption magnitude of 71.4 % and 56.4 % respectively and compare favorably to the simulation data. The deviation between simulation and experiment arises from using only estimated parameters for the materials properties [16].

Figure 2c shows the simulated absorption distribution in the x-z plane at the resonance frequency of 2.52 THz and reveals that the majority of the radiation is absorbed in the intermetal dielectric between M5 and M6 ERRs. In the x-y plane, Figure 2d shows that strong absorption occurs at the intersections of the M6 ERR cross arms. The simulated absorption distribution data revealed that the pn diode sensor is located ~ 8 µm beneath the region of maximum absorption. In order to determine the temperature change experienced by the pn diode sensor COMSOL multiphysics simulations were performed. A heat flux was injected in the intermetal dielectric region between M5 and M6, corresponding to the area of THz absorption, and the temperature rise on the pn silicon monitored. From Figure 3a it can be seen the heat is transferred into the lower CMOS layers to the silicon diodes.

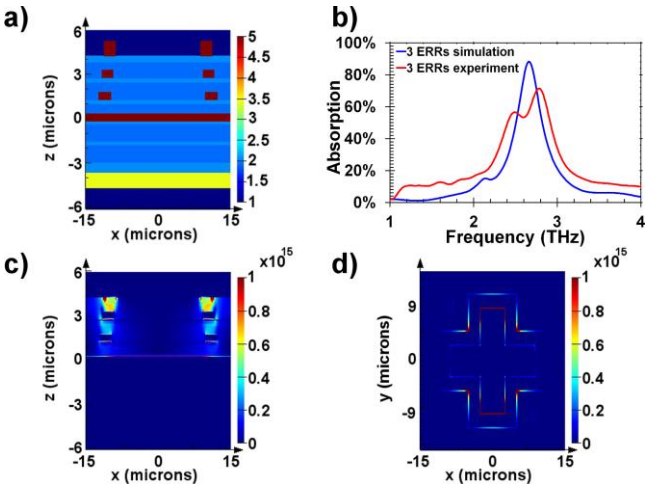

Fig. 2. a) Pixel cross-section showing the color-coded refractive index of the materials that comprise the MM absorber and diode microbolometer. b) Simulation (blue line) and experimental (red line) results of the THz MM absorber. c) Simulated THz power absorption distribution plot in the x-z plane at y = 0 µm. d) Simulated x-y power absorption distribution in the M6 layer.

Ideal diodes have a forward voltage of 0.7 V and a voltage change per degree of temperature, also called the temperature coefficient of voltage (TCV_D), of approximately -2 mV/K. The diode microbolometer sensitivity is lower than VOx microbolometers (~ 2 %/K) but can be improved by adding diodes in series in each pixel [20]. For this design, the number of diodes per pixel was decided based on two constraints: pixel size and maximum supply voltage of the CMOS technology (3.3 V). In order to maintain

compatibility with our previous MM designs [16,17], the pixel size was constrained to a 30 µm x 30 µm area resulting in three diodes in series per pixel according to the layout design rules for the specific CMOS technology.

A parameter analyzer (Keithley 4200-SCS) with 4 point probe measurements was used for I-V characterization, evaluation of the TCV_D and responsivity (R_v) measurements. Figure 3b shows the I-V characteristics for the experimental data compared to simulation. Both results show a turn on voltage of approximately 2.0 V for a current sweep from 0 A to 120 µA. The TCV_D was measured by placing the chip in an environmental chamber and sweeping the temperature from 10°C to 50°C while measuring the output voltage change at different bias currents (100 nA to 120 µA). Figure 3c shows the experimental TCV_D results compared to simulation at a current bias of 10 µA. The detectors showed an experimental TCV_D of -5.4 mV/K at 25°C for the three diodes in series.

The pixel's DC response, in terms of V/W, was measured from 10 nA to 120 µA on all three membrane thicknesses and was calculated using Eq. (1):

$$R_v = \frac{TCV_D \eta}{G_{th}\sqrt{1+\omega^2\tau^2}} \quad (1)$$

where TCV_D is the temperature coefficient of the diode forward voltage, η is the absorption coefficient, G_{th} is the thermal conductance, ω is the modulation frequency and τ is the thermal time constant [21].

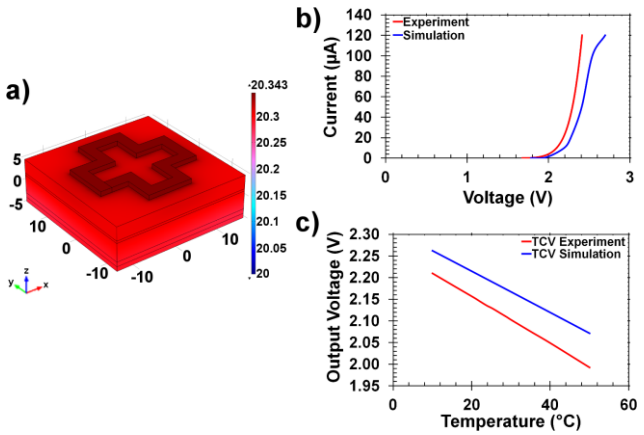

Fig. 3. a) COMSOL simulation results showing the heat distribution in the pixel. Experimental (red lines) versus simulation (blue lines) results showing the b) diode I-V characteristics and c) TCV_D.

Figure 4a shows the DC responsivity as a function of bias current for the three devices. Device B has the largest responsivity of 684 V/W while device C has the lowest responsivity of 79 V/W due to it having the largest thermal capacitance and a higher thermal conductance. The responsivity versus modulation frequency and the thermal time constant was determined by modulating the incident beam at different frequencies using an optical chopper and measuring the voltage difference on the THz sensor [17]. Figure 4b shows the responsivity of device B at different frequencies in the range of 1 Hz to 10 Hz at room temperature. The highest responsivity at 1 Hz is 274 V/W compared to the DC responsivity of 684 V/W at a bias current of 10 µA. The thermal time constant was derived from the responsivity versus frequency data and was found to be 420 ms. The noise spectral density (NSD) was measured by biasing the detectors at 10 µA and measuring the noise voltage using a dynamic signal analyzer (Agilent 35670A). The detectors were placed in a Faraday cage to reduce the external noise. The NSD was measured from 1 Hz to 10 kHz at room temperature. Figure 4c shows the NSD for device B (blue line) and device C (green line). The noise spectrum for the unetched chip, device C, shows both *1/f* and thermal noise components. The *1/f* noise is dominant at lower frequencies and the thermal noise dominates at larger frequencies. The etched chip shows a *1/f* noise behavior even at higher frequencies. This behavior is assigned to the introduction of defects during the plasma post-processing of the chip. The noise equivalent power (NEP) was calculated with the responsivity versus modulation frequency and NSD data using Eq. (2):

$$NEP = \frac{V_{rms}}{R_v} \quad (2)$$

where R_v is the responsivity and V_{rms} is the NSD. Figure 4b shows the NEP data (blue open symbols) from device B demonstrating a minimum NEP of 10.4 nW/√Hz at 5 Hz when biased at 10 µA. By using only one ERR so as to reduce the membrane from 9 µm to 4 µm and operating the detector under vacuum, previous work shows that the NEP could be decreased by up to two orders of magnitude [22].

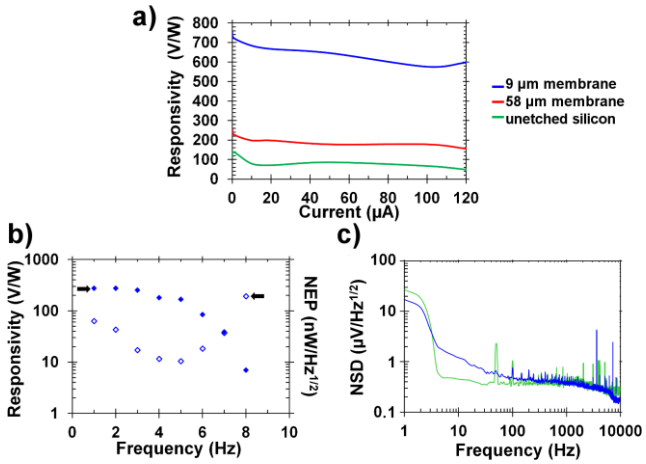

Fig. 4. a) DC Responsivity, R_v, as a function of bias current for three membrane thicknesses. b) Responsivity (solid symbols) and NEP (open symbols) as a function of modulation frequency for device B. c) NSD for device B (blue line) and device C (green line).

The diode sensor with the largest responsivity (device B) was used in transmission and reflection mode experiments to demonstrate its imaging capabilities using the aforementioned gas laser operating at 2.52 THz as the source. For both transmission and reflection, the incident beam was focused onto the object by a Tsupurica lens and the transmitted/reflected beam (1.5 mm spot size) was focused by a polymethylpentene (TPX) lens onto the THz sensor [17]. The optical images of the metallic object with a 'T' shape cut out are shown in Figure 5a when the object is uncovered and 5b when the object is covered by a manila envelope. The cut out 'T' shape had a length of 19 mm, height of 21 mm and arm

widths of 5 mm. The readout area was set to 25 mm x 25 mm with 1 mm x 1 mm resolution. Images were formed by raster-scanning the detector pixel in the x-y direction in 1 mm steps. The captured THz images obtained from the transmission mode experiment are shown in Figure 5c for the uncovered object and in Figure 5d for the covered object. The imaging experiment was repeated under the same conditions but in reflection mode using the same object. The stand-off distance was 15 cm and the object reflected the THz beam to the detector at an angle of 25°. Figure 5e shows the reflection image with the uncovered object and Figure 5f shows the image from the covered object. The four images were obtained by biasing the detector at 10 μA.

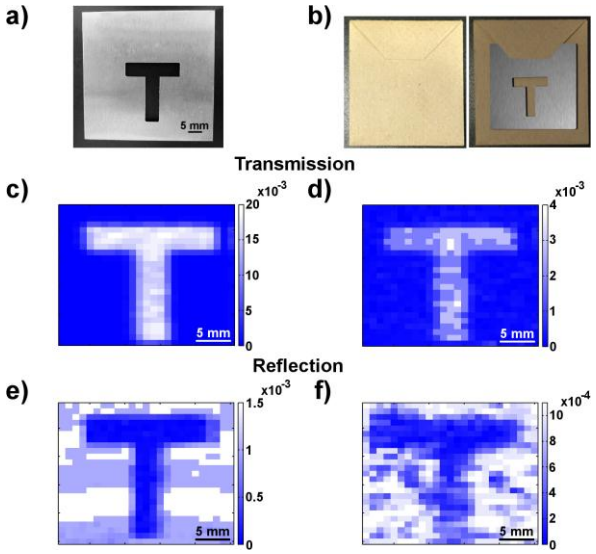

Fig. 5. a) Optical image of the metallic object with a 'T' shape cut out. b) Metallic object covered by a manila envelope. c) Transmission mode image of uncovered object and d) covered object. e) Reflection mode image of uncovered object and f) covered object.

We have demonstrated an uncooled CMOS THz imager comprised of a MM absorber and Si pn diode. Both the MM absorber and pn diode sensor were fabricated in a standard 180 nm CMOS process. The detector had a maximum responsivity of 684 V/W, a minimum NEP of 10.4 nW/√Hz and a thermal time constant of 420 ms. We demonstrated the detector's suitability for stand-off imaging applications by employing it in transmission and reflection mode imaging experiments to form images of a metallic object hidden in a manila envelope. Monolithic integration of the MM absorber and Si pn diode during the CMOS process reduces the fabrication complexity and cost compared to the present dominant technology, surface micro-machined microbolometers that are fabricated above the readout IC. Our technology has the advantage of scalability making it suitable for very low-cost and high resolution FPAs (e.g. 328 x 256). These advantages can lead to room temperature, real-time THz imaging systems. Furthermore, the operating frequency of the MM absorber can be tuned from the millimeter wave to the near IR by simply modifying the unit cell size and ERR dimension [23].

Funding. Engineering and Physical Sciences Research Council (EPSRC) (EP/I017461/1, EP/J018678/1).

Acknowledgment. We wish to acknowledge the contribution of the staff and facilities of the James Watt Nanofabrication Centre at Glasgow University, UK and Texas Instruments UK, Greenock, UK for provision of CMOS chips. The dataset associated with this research is available at [24].

REFERENCES

1. J. F. Federici, B. Schulkin, F. Huang, D. Gary, R. Barat, F. Oliveira, and D. Zimdars, Semicond. Sci. Technol. **20**, S266 (2005).
2. K. Kawase, Y. Ogawa, Y. Watanabe, and H. Inoue, Opt. Express **11**, 2549 (2003).
3. C. Yu, S. Fan, Y. Sun, and E. Pickwell-Macpherson, Quant. Imaging Med. Surg. **2**, 33 (2012).
4. F. Wahaia, I. Kasalynas, D. Seliuta, G. Molis, A. Urbanowicz, C. D. Carvalho Silva, F. Carneiro, G. Valusis, and P. L. Granja, J. Mol. Struct. **1079**, 448 (2015).
5. W. He, L. Zhang, D. Bowes, H. Yin, K. Ronald, A. D. R. Phelps, and A. W. Cross, Appl. Phys. Lett. **107**, 133501 (2015).
6. N. G. Gavrilov, B. A. Knyazev, E. I. Kolobanov, V. V Kotenkov, V. V Kubarev, G. N. Kulipanov, A. N. Matveenko, L. E. Medvedev, S. V. Miginsky, L. A. Mironenko, A. D. Oreshkov, V. K. Ovchar, V. M. Popik, T. V. Salikova, M. A. Scheglov, S. S. Serednyakov, O. A. Shevchenko, A. N. Skrinsky, V. G. Tcheskidov, and N. A. Vinokurov *et al.*, Nucl. Instruments Methods Phys. Res. Sect. A **575**, 54 (2007).
7. A. Khalid, G. M. Dunn, R. F. Macpherson, S. Thoms, D. Macintyre, C. Li, M. J. Steer, V. Papageorgiou, I. G. Thayne, M. Kuball, C. H. Oxley, M. Montes Bajo, A. Stephen, J. Glover, and D. R. S. Cumming, J. Appl. Phys. **115**, 114502 (2014).
8. K. Statnikov, J. Grzyb, B. Heinemann, and U. R. Pfeiffer, IEEE Trans. Microwave Theory Tech. **63**, 520 (2015).
9. B. S. Williams, S. Kumar, Q. Hu, and J. L. Reno, Electron. Lett. **42**, 89 (2006).
10. R. Han, Y. Zhang, Y. Kim, D. Y. Kim, H. Shichijo, E. Afshari, and K. O. Kenneth, IEEE J. Solid-State Circuits **48**, 2296 (2013).
11. H. Sherry, J. Grzyb, Z. Yan, R. Al Hadi, A. Cathelin, A. Kaiser, and U. Pfeiffer, in *IEEE Solid-State Circuits Conference* Digest of Technical Papers (ISSCC), San Francisco, CA, 2012, pp. 252-254.
12. M. Bauer, R. Venckevičius, I. Kašalynas, S. Boppel, M. Mundt, L. Minkevičius, A. Lisauskas, G. Valušis, V. Krozer, and H. G. Roskos, Opt. Express **22**, 19250 (2014).
13. J. Oden, J. Meilhan, J. Lalanne-Dera, J. F. Roux, F. Garet, J. L. Coutaz, and F. Simoens, Opt. Express **21**, 4817 (2013).
14. N. Oda, T. Ishi, S. Kurashina, T. Sudou, T. Morimoto, M. Miyoshi, K. Doi, H. Goto, T. Sasaki, G. Isoyama, R. Kato, A. Irizawa, and K. Kawase, Proc. SPIE **9483**, 94830S (2015).
15. D. Dufour, L. Marchese, M. Terroux, H. Oulachgar, F. Généreux, M. Doucet, L. Mercier, B. Tremblay, C. Alain, P. Beaupré, N. Blanchard, M. Bolduc, C. Chevalier, D. D'Amato, Y. Desroches, F. Duchesne, L. Gagnon, S. Ilias, H. Jerominek, F. Lagacé, J. Lambert, F. Lamontagne, L. Le, Noc, A. Martel, O. Pancrati, J.-E. Paultre, T. Pope, F. Provençal, P. Topart, C. Vachon, S. Verreault, and A. Bergeron, J. Infrared Millimeter Terahertz Waves **36**, 922 (2015).
16. J. Grant, I. Escorcia-Carranza, C. Li, I. J. H. McCrindle, J. Gough, and D. R. S. Cumming, Laser Photon. Rev. **7**, 1043 (2013).
17. I. E. Carranza, J. Grant, J. Gough, and D. R. S. Cumming, Terahertz Sci. Technol. IEEE Trans. **5**, 892 (2015).
18. J. Grant, Y. Ma, S. Saha, L. B. Lok, A. Khalid, and D. R. S. Cumming, Opt. Lett. **36**, 1524 (2011).
19. J. Grant, Y. Ma, S. Saha, A. Khalid, and D. R. S. Cumming, Opt. Lett. **36**, 3476 (2011).
20. D. B. Etter, S. Sun, F. X. Hutter, J. N. Burghartz, F. Utermohlen, and I. Herrmann, *International Semiconductor Conference Dresden – Grenoble (ISCDG)* (2013), p. 1.

21. F. Niklaus, A. Decharat, C. Jansson, and G. Stemme, Infrared Phys. Technol. **51**, 168 (2008).
22. F. Niklaus, C. Jansson, A. Decharat, J.-E. Källhammer, H. Pettersson, and G. Stemme, Proc. SPIE **6542**, 65421M (2007).
23. J. Grant, I. J. H. McCrindle, and D. R. S. Cumming, Opt. Express **24**, 3451 (2016).
24. http://dx.doi.org/10.5525/gla.researchdata.314

REFERENCES

1. J. F. Federici, B. Schulkin, F. Huang, D. Gary, R. Barat, F. Oliveira, and D. Zimdars, "THz imaging and sensing for security applications—explosives, weapons and drugs," Semicond. Sci. Technol. 20, S266–S280 (2005).
2. K. Kawase, Y. Ogawa, Y. Watanabe, and H. Inoue, "Non-destructive terahertz imaging of illicit drugs using spectral fingerprints," Opt. Express 11, 2549–2554 (2003).
3. C. Yu, S. Fan, Y. Sun, and E. Pickwell-Macpherson, "The potential of terahertz imaging for cancer diagnosis: A review of investigations to date.," Quant. Imaging Med. Surg. 2, 33–45 (2012).
4. F. Wahaia, I. Kasalynas, D. Seliuta, G. Molis, A. Urbanowicz, C. D. Carvalho Silva, F. Carneiro, G. Valusis, and P. L. Granja, "Study of paraffin-embedded colon cancer tissue using terahertz spectroscopy," J. Mol. Struct. 1079, 448–453 (2015).
5. W. He, L. Zhang, D. Bowes, H. Yin, K. Ronald, A. D. R. Phelps, and A. W. Cross, "Generation of broadband terahertz radiation using a backward wave oscillator and pseudospark-sourced electron beam," Appl. Phys. Lett. 107, 133501 (2015).
6. N. G. Gavrilov, B. A. Knyazev, E. I. Kolobanov, V. V Kotenkov, V. V Kubarev, G. N. Kulipanov, A. N. Matveenko, L. E. Medvedev, S. V Miginsky, L. A. Mironenko, A. D. Oreshkov, V. K. Ovchar, V. M. Popik, T. V Salikova, M. A. Scheglov, S. S. Serednyakov, O. A. Shevchenko, A. N. Skrinsky, V. G. Tcheskidov, and N. A. Vinokurov, "Status of the Novosibirsk high-power terahertz FEL," Nucl. Instruments Methods Phys. Res. Sect. A Accel. Spectrometers, Detect. Assoc. Equip. 575, 54–57 (2007).
7. A. Khalid, G. M. Dunn, R. F. Macpherson, S. Thoms, D. Macintyre, C. Li, M. J. Steer, V. Papageorgiou, I. G. Thayne, M. Kuball, C. H. Oxley, M. Montes Bajo, A. Stephen, J. Glover, and D. R. S. Cumming, "Terahertz oscillations in an In0.53Ga0.47As submicron planar Gunn diode," J. Appl. Phys. 115, 114502 (2014).
8. K. Statnikov, J. Grzyb, B. Heinemann, and U. R. Pfeiffer, "160-GHz to 1-THz Multi-Color Active Imaging With a Lens-Coupled SiGe HBT Chip-Set," Microw. Theory Tech. IEEE Trans. 63, 520–532 (2015).
9. B. S. Williams, S. Kumar, Q. Hu, and J. L. Reno, "High-power terahertz quantum-cascade lasers," Electron. Lett. 42, 89–91 (2006).
10. R. Han, Y. Zhang, Y. Kim, D. Y. Kim, H. Shichijo, E. Afshari, and K. K. O, "Active terahertz imaging using schottky diodes in CMOS: Array and 860-ghz pixel," IEEE J. Solid-State Circuits 48, 2296–2308 (2013).
11. H. Sherry, J. Grzyb, Y. Zhao, R. Al Hadi, A. Cathelin, A. Kaiser, and U. Pfeiffer, "A 1kpixel CMOS camera chip for 25fps real-time terahertz imaging applications," in IEEE International Solid-State Circuits Conference Digest of Technical Papers (ISSCC) (IEEE, 2012), pp. 252–254.
12. M. Bauer, R. Venckevičius, I. Kašalynas, S. Boppel, M. Mundt, L. Minkevičius, A. Lisauskas, G. Valušis, V. Krozer, H. G. Roskos, "Antenna-coupled field-effect transistors for multi-spectral terahertz imaging up to 4.25 THz.," Opt. Express 22, 19250–19256 (2014).
13. J. Oden, J. Meilhan, J. Lalanne-Dera, J. F. Roux, F. Garet, J. L. Coutaz, and F. Simoens, "Imaging of broadband terahertz beams using an array of antenna-coupled microbolometers operating at room temperature," Opt. Express 21, 4817–4825 (2013).
14. N. Oda, T. Ishi, S. Kurashina, T. Sudou, T. Morimoto, M. Miyoshi, K. Doi, H. Goto, T. Sasaki, G. Isoyama, R. Kato, A. Irizawa, and K. Kawase, "Performances of THz cameras with enhanced sensitivity in sub-terahertz region," SPIE Terahertz Physics, Devices, Syst. IXAdvanced Appl. Ind. Def. 9483, 94830S (2015).
15. D. Dufour, L. Marchese, M. Terroux, H. Oulachgar, F. Généreux, M. Doucet, L. Mercier, B. Tremblay, C. Alain, P. Beaupré, N. Blanchard, M. Bolduc, C. Chevalier, D. D'Amato, Y. Desroches, F. Duchesne, L. Gagnon, S. Ilias, H. Jerominek, F. Lagacé, J. Lambert, F. Lamontagne, L. Le Noc, A. Martel, O. Pancrati, J.-E. Paultre, T. Pope, F. Provençal, P. Topart, C. Vachon, S. Verreault, and A. Bergeron, "Review of terahertz technology development at INO," J. Infrared, Millimeter, Terahertz Waves 36, 922–946 (2015).
16. J. Grant, I. Escorcia-Carranza, C. Li, I. J. H. McCrindle, J. Gough, and D. R. S. Cumming, "A monolithic resonant terahertz sensor element comprising a metamaterial absorber and micro-bolometer," Laser Photon. Rev. 7, 1043–1048 (2013).
17. I. E. Carranza, J. Grant, J. Gough, and D. R. S. Cumming, "Metamaterial-Based Terahertz Imaging," Terahertz Sci. Technol. IEEE Trans. 5, 892–901 (2015).
18. J. Grant, Y. Ma, S. Saha, L. B. Lok, A. Khalid, and D. R. S. Cumming, "Polarization insensitive terahertz metamaterial absorber," Opt. Lett. 36, 1524–1526 (2011).
19. J. Grant, Y. Ma, S. Saha, A. Khalid, and D. R. S. Cumming, "Polarization insensitive, broadband terahertz metamaterial absorber," Opt. Lett. 36, 3476–3478 (2011).
20. D. B. Etter, S. Sun, F. X. Hutter, J. N. Burghartz, F. Utermohlen, and I. Herrmann, "Microbolometer technology using serial pn-diodes," 2013 IEEE Int. Semicond. Conf. Dresden - Grenoble Technol. Des. Packag. Simul. Test, ISCDG 2013 1–4 (2013).
21. F. Niklaus, A. Decharat, C. Jansson, and G. Stemme, "Performance model for uncooled infrared bolometer arrays and performance predictions of bolometers operating at atmospheric pressure," Infrared Phys. Technol. 51, 168–177 (2008).
22. F. Niklaus, C. Jansson, A. Decharat, J.-E. Källhammer, H. Pettersson, and G. Stemme, "Uncooled infrared bolometer arrays operating in a low to medium vacuum atmosphere: performance model and tradeoffs," Soc. Photo-Optical Instrum. Eng. Conf. Ser. 6542, 65421M–65421M–12 (2007).
23. J. Grant, I. J. H. McCrindle, and D. R. S. Cumming, "Multi-spectral materials: hybridisation of optical plasmonic filters, a mid infrared metamaterial absorber and a terahertz metamaterial absorber," Opt. Express 24, 3451 (2016).